Nuclear Science and Techniques (2024) 35:175
https://doi.org/10.1007/s41365-024-01526-x

Analysis and optimization of performance parameters of the ^{220}Rn chamber in flow-field mode using computational fluid dynamics method

Shao-Hua Hu[1] · Yong-Jun Ye[2] · Zheng-Zhong He[1] · De-Tao Xiao[1] · Xiang-Yu Xu[1] · Jian-Kai Wang[1] · Qing-Zhi Zhou[1]

Received: 26 December 2023 / Revised: 9 March 2024 / Accepted: 23 March 2024 / Published online: 24 September 2024

Abstract
The impact of the radiation dose produced by ^{222}Rn/^{220}Rn and its progeny on human health has garnered increasing interest in the nuclear research field. The establishment of robust, regulatory, and competent ^{220}Rn chambers is crucial for accurately measuring radioactivity levels. However, studying the uniformity of the ^{220}Rn progeny through experimental methods is challenging, because measuring the concentration of ^{220}Rn and its progeny in multiple spatial locations simultaneously and in real time using experimental methods is difficult. Therefore, achieving precise control of the concentration of ^{220}Rn and its progeny as well as the reliable sampling of the progeny pose significant challenges. To solve this problem, this study uses computational fluid dynamics to obtain the flow-field data of the ^{220}Rn chamber under different wind speeds and progeny-replenishment rates. Qualitative analysis of the concentration distribution of the progeny and quantitative analysis of the progeny concentration and uniformity of the progeny concentration are conducted. The research findings indicated that the progeny concentration level is primarily influenced by wind speed and the progeny-complement rate. Wind speed also plays a crucial role in determining progeny concentration uniformity, whereas the progeny-complement rate has minimal impact on uniformity. To ensure the accuracy of ^{220}Rn progeny concentration sampling, we propose a methodology for selecting an appropriate sampling area based on varying progeny concentrations. This study holds immense importance for enhancing the regulation and measurement standards of ^{220}Rn and its progeny.

Keywords Thoron · Progeny · Regulatory · CFD simulation

1 Introduction

The decay products of radon (^{222}Rn) and thoron (^{220}Rn) are particulates and are deposited in the lungs upon inhalation, causing internal irradiation. This may lead to DNA damage, resulting in the induction of lung cancer under prolonged exposure [1–4]. Radon and thoron have considerable radiological importance as the inhalation of these gases and their short-lived progeny constitute the most significant fraction (52%) of the radiation dose to humans from natural sources [5]. Thorium resources are abundant worldwide [6, 7], and the development of thorium-based nuclear-fuel technology is ongoing. To reduce radiation levels and sustainably use thorium resources, creating scientific devices to measure and evaluate ^{220}Rn and its progeny is important. This will lay the groundwork for the development of measurement instruments and tools for ^{220}Rn and their progeny [8–10].

In recent years, research on the regulation of ^{220}Rn chambers has been conducted globally [11, 12]. However, maintaining a constant long-term concentration of ^{220}Rn and its progeny in the ^{220}Rn chamber is difficult because their half-lives differ. Additionally, the deposition and

This work was supported by the National Natural Science Foundation of China (Nos. 12375310, 12175102, and 118750356), Youth Talent Foundation of Hunan Province of China (2022TJ-Q16), and Graduate Research and Innovation Projects of Hunan Province (CX20230964).

✉ Qing-Zhi Zhou
zhouqingzhi2005@163.com

[1] School of Nuclear Science and Technology, University of South China, Hengyang 421001, China

[2] School of Resources Environment and Safety Engineering, University of South China, Hengyang 421001, China

attachment of ^{220}Rn progeny are evident, further contributing to the lack of uniformity in ^{220}Rn and its progeny concentration within the chamber [9, 10, 13]. The uniformity of the ^{220}Rn progeny concentration is an important index of sampling reliability, but many difficulties have been encountered in related research. (1) The traditional experimental method fails to address the challenge of simultaneously measuring the concentration of ^{220}Rn progeny at various spatial points within the ^{220}Rn chamber. Consequently, experimentally examining the uniformity of the ^{220}Rn progeny concentration becomes unfeasible. (2) Because of the long time required for the ^{220}Rn progeny concentration measurement, which takes over 2 h, the experimental measurement data have a certain lag. Therefore, a novel approach is required to acquire physical information on the flow field within the ^{220}Rn chamber to enhance the uniformity of the progeny concentration and improve the reliability of ^{220}Rn progeny sampling.

Computational fluid dynamics (CFD) is a highly effective tool used in the aerospace [14, 15], automobile [16, 17], shipbuilding [18–20], and chemical industries [21, 22], as well as in aerosol science and technology [23–26]. Recently, CFD has also been applied to study the migration of radioactive aerosols in limited spaces [27–35]. Agarwal et al. [27] simulated the effect of ventilation rate on the ^{220}Rn concentration distribution in a test house. This study broadened the potential use of the CFD technique to handle the expected variability in the ^{220}Rn concentration profile. In addition, Agarwal et al. [3] developed a comprehensive CFD code to investigate the behavior of ^{222}Rn/^{220}Rn and its progeny in indoor environments, thereby confirming its reliability and authenticity. This study also demonstrated the applicability of a CFD code for analyzing the distribution of ^{220}Rn concentration in an experimental chamber. In addition to the aforementioned research, studies conducted by P. M. et al. [34] and Jun et al. [35] significantly advanced the application of CFD in the investigation of radioactive aerosols. Agarwal [3] introduced the volume-deposition rate to simulate the loss of the ^{222}Rn progeny that is deposited near the wall owing to gravity and other factors and then attached to the wall surface. However, because the volume-deposition rate is an averaged parameter, studying the concentration distribution of the ^{220}Rn progeny using it will not yield results that are sufficiently accurate. By utilizing CFD, the migration process of radioactive aerosols in a ^{220}Rn chamber may be replicated, and the distribution of radioactive aerosol concentrations can be determined, as demonstrated in these studies. Hence, using CFD to simulate the migration process of ^{220}Rn progeny in a ^{220}Rn chamber and analyze their temporal-spatial distribution is a viable approach to address the limitations of experimental methods in monitoring the concentration levels of progeny across multiple spatial locations simultaneously. This method can potentially improve the uniformity of ^{220}Rn and its progeny concentration.

This article introduces the basic structure of a ^{220}Rn chamber in Sect. 2 and establishes a numerical model based on fluid mechanics under the flow-field pattern of the ^{220}Rn chamber in combination with the decay law of the ^{220}Rn progeny and the law of the ^{220}Rn progeny deposition on the wall. Section 3 analyzes the effects of wind speed and progeny-complement rate on the ^{220}Rn progeny concentration distribution, with a focus on analyzing the relationship between the wind speed and progeny-complement rate at the level of the ^{220}Rn progeny concentration and the uniformity of progeny concentration. Based on the conclusions, Sects. 3 and 4 comprehensively analyze the regulation of the wind speed and progeny-complement rate on the progeny concentration level and guides the selection of sampling areas under different ^{220}Rn progeny concentration levels. The conclusions of this study provide theoretical guidance for the regulation of ^{220}Rn progeny concentration levels and the reliable sampling of the ^{220}Rn progeny concentration in a ^{220}Rn chamber.

2 Theoretical descriptions

2.1 ^{220}Rn chamber

^{220}Rn chambers are standard devices that provide a consistent and stable atmospheric environment with a specific concentration of ^{220}Rn and its progeny. Figure 1 illustrates the two main components of the device: the aging and calibration chambers. The aging chamber continuously replenishes the ^{220}Rn progeny such as the attached ^{212}Pb and ^{212}Bi to compensate for the consumption of the ^{220}Rn progeny by the ^{220}Rn chamber. The performance of the aging chamber has been reported in detail [36]; therefore, this study focuses solely on the calibration chamber without considering the aging chamber. The progeny-complement rate is the flow rate of air containing attached ^{212}Pb and ^{212}Bi supplemented at the inlet.

Figure 1 shows that, in addition to the aging and calibration chambers, the ^{220}Rn chamber also includes a fan and several circulating pipes. The fan aims to accelerate the ^{220}Rn progeny concentration to a uniform level by adjusting its wind speed. The fluid within the ^{220}Rn chamber flows in a clockwise direction. In addition, two sampling areas exist in the calibration room, namely sampling areas 1 and 2, which are numbered S_1 and S_2, respectively. Sampling area S_1 is at the center of the calibration room of the ^{220}Rn chamber, and sampling area S_2 is 0.20m to the left of sampling area S_1. Among them, the flow field in sampling area S_1

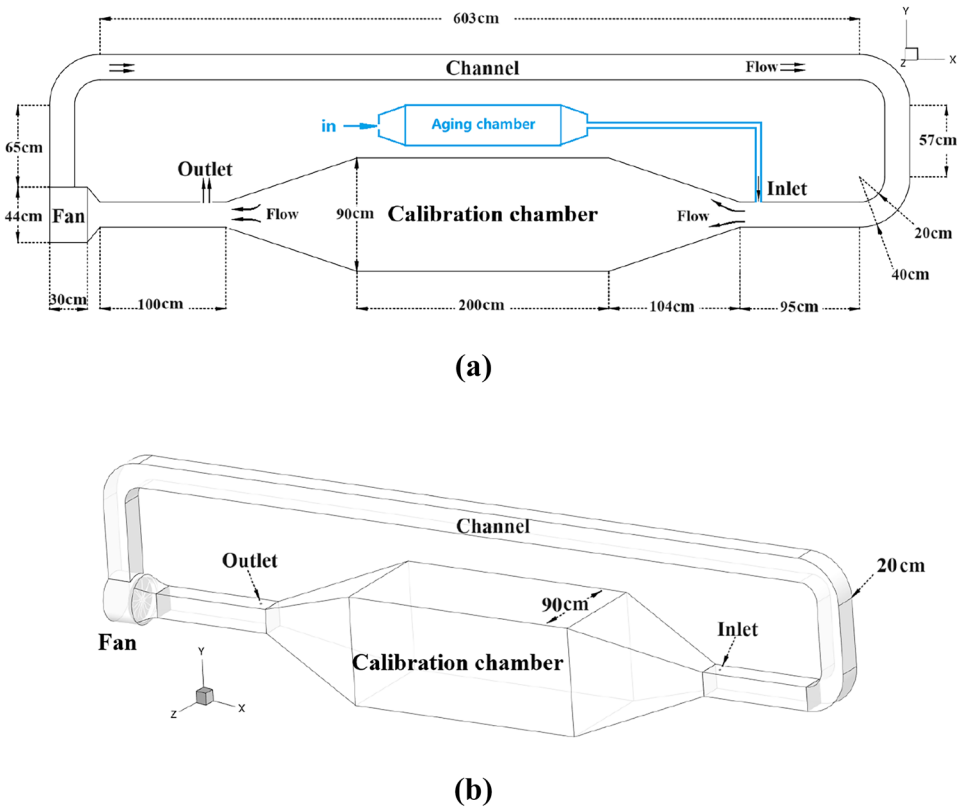

Fig. 1 Schematic representation of the **a** 2D and **b** 3D structures of the ^{220}Rn chamber

is more stable, which is suitable for sampling progeny with various flow rates and belongs to the preferred sampling area, whereas the concentration uniformity of the progeny in sampling area S_2, which is the standby sampling area, is marginally better.

2.2 Simulation procedure

2.2.1 Governing equations

A CFD software based on the finite volume method was employed to simulate the concentration distribution of the attached ^{212}Pb and ^{212}Bi within the ^{220}Rn chamber. Mass- and momentum-conservation equations were used to model the flow-field mode. Then, various modules/equations describing the relevant physical processes governing the attached ^{212}Pb and ^{212}Bi are incorporated using a user-defined function to simulate the concentration distribution of the attached ^{212}Pb and ^{212}Bi in the ^{220}Rn chamber. The predictive accuracy of this software was previously validated in various contexts [27].

In the simulation, the flow was assumed continuous and incompressible. The temperature inside the ^{220}Rn chamber was considered constant and uniform and was set at 300 K. The governing equations for the mass and momentum conservation are as follows [28–30, 37]:

$$\frac{\partial \rho}{\partial t} + \frac{\partial (\rho u_i)}{\partial x_i} = 0, \tag{1}$$

$$\frac{\partial (\rho u_i)}{\partial t} + \frac{\partial (\rho u_i u_j)}{\partial x_i} = -\frac{\partial P}{\partial x_i} + \frac{\partial \mu \left(\frac{\partial u_i}{\partial x_j} + \frac{\partial u_j}{\partial x_i} \right)}{\partial x_j}, \tag{2}$$

where ρ is the fluid density (kg m^{-3}), t is the fluid time (s), x_i is the spatial coordinates (m) with the numbering index x_i = 1, 2, 3 for x, y, and z, respectively, u_i is the velocity vector (m s^{-1}) with the numbering index i=1, 2, 3 for u, v, and w, respectively, P is the pressure (N m^{-2}), and μ is the fluid viscosity.

The release of β- and γ-rays does not generate sufficient recoil kinetic energy to free the ^{220}Rn progeny from aerosols during the decay of ^{212}Pb to ^{212}Bi. Therefore, the impact of the recoil variables was not considered in this study. The activity concentration distribution of the ^{220}Rn progeny in the ^{220}Rn chamber is as follows [30, 37]:

$$\frac{\partial C_i}{\partial t} + \nabla \cdot ((U + v_s) C_i) = \nabla \cdot (D_e \nabla C_i) + \lambda_{i-1} C_{i-1} - \lambda_i C_i, \tag{3}$$

where the numbering indices are i = 1, 2 for the attached ^{212}Pb and ^{212}Bi, respectively. U is the mean velocity (m s^{-1}), D_e is the effective diffusion coefficient (m^2 s^{-1}), C_i is the activity concentration (Bq m^{-3}) of the ith decay product, λ_i is

the decay constant (s^{-1}) of the ith decay product. In Eq. (3), the parameters are estimated using the appropriate mathematical models, as discussed below. The decay constants (λ_i) are $\lambda_{^{212}\mathrm{Pb}} = 1.8 \times 10^{-5}\ s^{-1}$ and $\lambda_{^{212}\mathrm{Bi}} = 1.9 \times 10^{-4}\ s^{-1}$. v_s is the settling velocity (m s^{-1}) from which the Stokes law can be obtained.

$$v_s = \frac{2r^2 g}{9\mu}(\rho_0 - \rho), \tag{4}$$

where r is the radius of the particle (m); the radius of the aerosol particles is set to 100 nm. ρ_0 denotes the particle density (kg m^{-3}).

The effective diffusion coefficient D_e is the sum of the Brownian diffusion coefficient (D_b) and turbulent diffusion coefficient (D_t). The diffusion coefficient (D_b) is calculated using the Stokes–Einstein relationship:

$$D_b = \frac{K_b T C_u}{6\pi\mu r}, \tag{5}$$

where C_u denotes the Cunningham slip correction factor that is calculated as follows [37, 38]:

$$C_u = 1 + \frac{l_m}{2r}\left(2.34 + 1.05e^{-0.39\frac{d}{l_m}}\right), \tag{6}$$

where k_b is the Boltzmann constant ($m^2\ kg\ s^{-2}\ K^{-1}$), l_m is the mean free path of the air molecules (m), μ is the viscosity of air (Pa s), and T is the temperature (K).

2.2.2 Turbulence model

During the operation of the ^{220}Rn chamber, when the fan operates at its lowest power setting, the minimum Reynolds number is approximately 2500. As the wind speed increases, the entire ^{220}Rn chamber becomes turbulent. Consequently, this study chose the standard $\kappa - \varepsilon$ model to conduct the simulation calculations. This equation is expressed as follows:

$$\frac{\partial(\rho\kappa)}{\partial t} + \frac{\partial(\rho\kappa u_i)}{\partial x_i} = \frac{\partial\left(\left(\mu + \frac{\mu_t}{\sigma_\kappa}\right)\frac{\kappa}{x_j}\right)}{\partial x_j} + G_\kappa - \rho\varepsilon, \tag{7}$$

$$\frac{\partial(\rho\varepsilon)}{\partial t} + \frac{\partial(\rho\varepsilon u_i)}{\partial x_i} = \frac{\partial\left(\left(\mu + \frac{\mu_t}{\sigma_\varepsilon}\right)\frac{\varepsilon}{x_j}\right)}{\partial x_j} + \rho C_1 E\varepsilon - \rho C_2 \frac{\varepsilon^2}{\kappa + \sqrt{\nu\varepsilon}}, \tag{8}$$

where μ_t is the turbulent-flow velocity, G_κ is the generation term of the turbulent kinetic energy κ owing to the average velocity gradient, σ_κ and σ_ε are the Prandtl numbers corresponding to the turbulent kinetic energy κ and dissipation rate σ, respectively, and C_1 and C_2 are constants: $C_1 = 1.44$, $C_2 = 1.92$.

2.3 Initial and boundary conditions

The airflow was selected along the direction perpendicular to the inlet for the simulations. According to Li et al. [36], the concentration and velocity of the attached progeny at the inlet are set by Eqs. (9) and (10). The outlet is set as the pressure outlet. To generate a dynamic flow field, the rotating shaft of the fan is set along the x-axis. No-slip and adiabatic conditions were imposed on the walls of the computational domain.

$$C^{\mathrm{inlet}}_{^{212}\mathrm{Pb}} = \frac{1.99 \times 10^7}{(1.647 + Q)(334.35 + Q)}\ \mathrm{Bq/m^3}, \tag{9}$$

$$C^{\mathrm{inlet}}_{^{212}\mathrm{Bi}} = \frac{1.03 \times 10^7}{(1.647 + Q)(334.35 + Q)(6.3315 + Q)}\ \mathrm{Bq/m^3}, \tag{10}$$

where $C^{\mathrm{inlet}}_{^{212}\mathrm{Pb}}$ is the concentration of the attached ^{212}Po at the inlet, $C^{\mathrm{inlet}}_{^{212}\mathrm{Bi}}$ is the concentration of the attached ^{212}Bi at the inlet, and Q is the progeny-complement rate (L min^{-1}).

To address the phenomenon of the indoor deposition and wall attachment of ^{220}Rn progeny, the volume-deposition rate is commonly used to represent the loss of progeny due to deposition and wall attachment [33]. The volume-deposition rate is a macroscopic effect of the overall loss of the ^{220}Rn progeny and is a volume-averaged concept. To solve the error caused by the volume-deposition rate, the surface-deposition rate is used to replace the volume-deposition rate, and the phenomenon of ^{220}Rn progeny deposition is set near the wall of the ^{220}Rn chamber. In this simulation, a grid layer on the ^{220}Rn wall is extracted as the area where the ^{220}Rn progeny is deposited on the wall. In this area, the source term is set to realize the deposition of the ^{220}Rn progeny on the surface of the ^{220}Rn chamber. The source-parameter surface-deposition rate has the following relationship:

$$S_{\mathrm{wd}} = -\lambda_{\mathrm{wd}} \cdot C_i, \tag{11}$$

where S_{wd} is the ^{220}Rn progeny-deposition source term, λ_{wd} is the deposition rate (s^{-1}) to the surface. The volume-deposition rate (λ_{Vd}) acts on the entire ^{220}Rn chamber, and the wall deposition rate (λ_{wd}) acts on the area near the wall in the simulation calculation. The formula can be expressed as

$$\lambda_{\mathrm{wd}} = \lambda_{\mathrm{Vd}}\frac{V_0}{V_W} + D, \tag{12}$$

where V_0 is the volume of the ^{220}Rn chamber, V_W is the volume of the area where the surface-deposition rate occurs, and D is the error coefficient.

2.4 Meshing

2.4.1 Grid setting at boundary

To reduce the backflow at the inlet and outlet, they were extended by 10cm. In this study, the grid is formed using hexahedral and tetrahedral methods, in which the fan, inlet, and outlet areas are tetrahedral grids, and the other areas are hexahedral grids. The flow field in the fan area is complex; thus, in this study local encryption is performed for the fan area. The total number of grids in the ^{220}Rn chamber is approximately 586 000. The grid quality was evaluated using the orthogonal quality, and the orthogonal quality average was 0.81279. The mesh is illustrated in Fig. 2a. Based on the boundary conditions described in Sect. 2.3, the deposition area was set near the wall. In this study, a grid layer near the wall was recorded as the deposition area. Figure 2b shows the deposition area setting of the $x = 0$ plane, where the outermost light-yellow area is the deposition area.

2.4.2 Grid-independence test

In this study, a grid-independence test experiment was conducted with grid numbers of 295 000 and 788 000. In this experiment, the wind speed and concentration of ^{220}Rn progeny at C22 in the ^{220}Rn chamber were compared. *M*1, *M*2, and *M*3 represent grid numbers of 295 000, 586 000, and 788 000, respectively. The following results are shown in Fig. 3: (1) in the experiment comparing the wind speed of three kinds of grid flow fields, the relative deviation of wind speed at C22 in the ^{220}Rn room is 3.18%; (2) an experiment on the changes of ^{212}Pb and ^{212}Bi concentrations with time was conducted under the condition of a wind speed of 0.05 m/s and progeny-complement rate of 7 L/min. When the progeny concentration of ^{220}Rn in the ^{220}Rn chamber reached a steady state, the relative deviation in the progeny concentration of ^{220}Rn was 1.25%. This grid-independence test showed that with an increase in the number of grids, the consistency of the concentration-change law of the ^{220}Rn progeny is good, and the flow field inside the ^{220}Rn chamber exhibits little change, which proves that the number of grids set in this study is appropriate.

2.5 Experimental methodology

2.5.1 Decay products of ^{220}Rn concentration measurements

In this study, the decay products of thoron inside the ^{220}Rn chamber were measured using an alpha-spectrometer method based on alpha spectroscopy. The measurement procedure involved sampling the decay products of thoron (^{220}Rn) using a microporous membrane and self-made sampling rod. The structure of the sampling rod, illustrated in Fig. 4, includes a head, microporous membrane, metal mesh, washer, and thread. The tail of the sampling rod is a long metal rod. The figure shows that microporous membranes, metal meshes, and washers are stacked in sequence in the structure head, and the head and thread are connected to form the structure of the sampling head. The sampling-rod samples from the ^{220}Rn chamber using an air pump, the air containing the ^{220}Rn progeny enters the sampler through the head and then passes through microporous membrane, and the ^{220}Rn progeny is adsorbed on the microporous membrane. Then, it passes through the metal mesh, which mainly prevents the microporous membrane from being broken

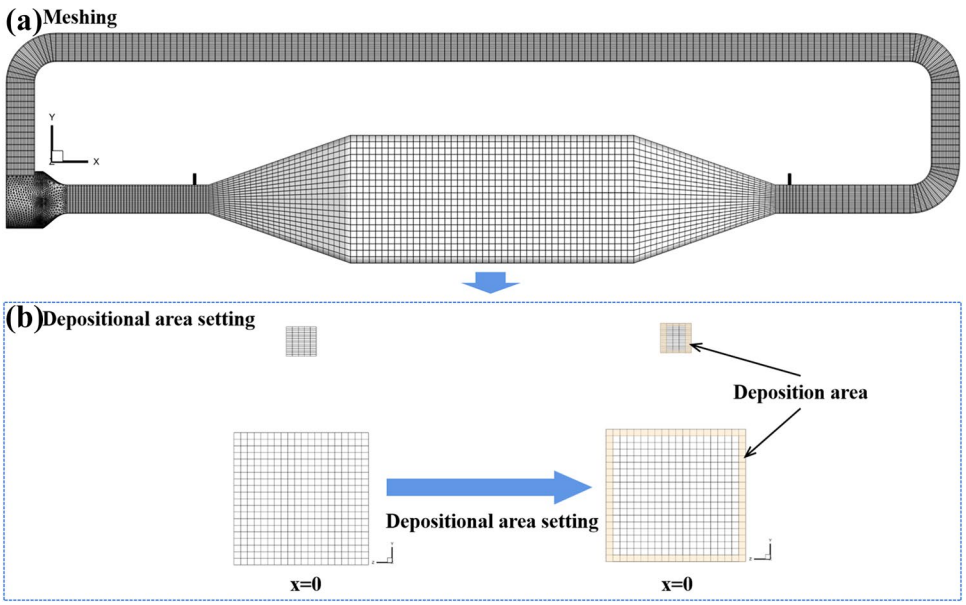

Fig. 2 (Color online) Schematic of **a** meshing and **b** depositional area setting of ^{220}Rn chamber

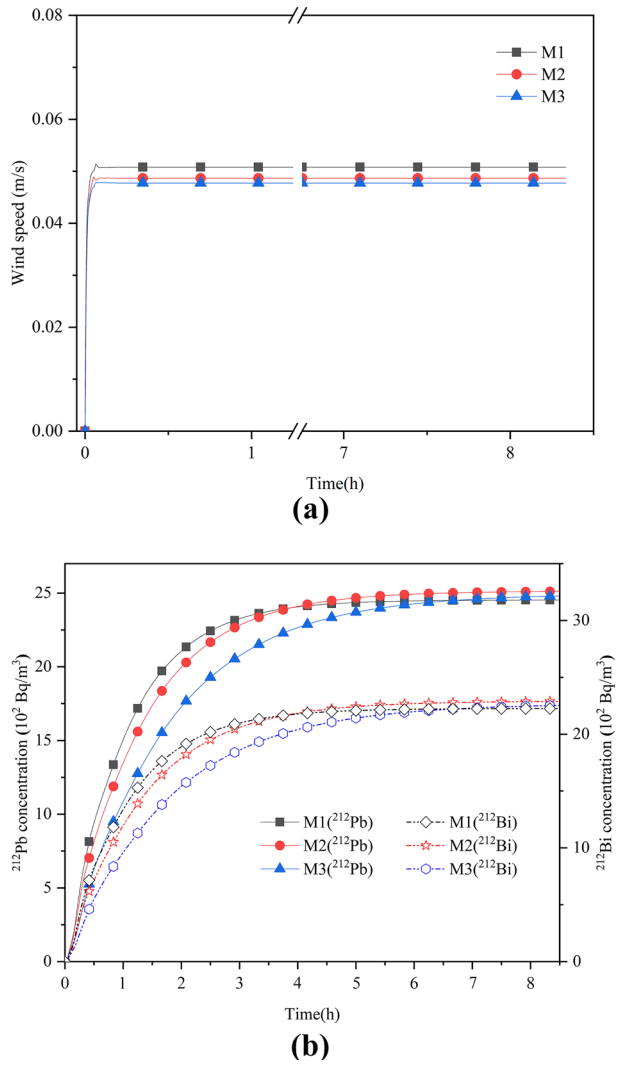

Fig. 3 Comparison of **a** wind speed and **b** progeny concentration with the change of grid number

owing to excessive sampling airflow. A washer is used to ensure that microporous membrane and metal mesh are tightly attached to the structure head, ensuring that the airflow passed through the microporous membrane. The structure duct is approximately 70 cm long and can be sampled at different positions along the axis of the ^{220}Rn chamber-sampling hole. The rear end of the structural duct can be connected to a pipe to reintroduce gas into the ^{220}Rn chamber.

During the sampling process, the ^{220}Rn progeny concentration was first sampled for 10 min at a sampling flow rate of 5L/min, and the sampled filter film was then placed in an alpha spectrometer for counting. Counts N_1 and N_2 were obtained by measuring the 8.78 MeV energy-peak counts of ^{212}Po using the α-spectrum approach [9, 36]. Finally, the activity concentrations of attached ^{212}Pb and ^{212}Bi were determined using Eqs. (12) and (13). The measurement procedure for the progeny concentration is shown in Fig. 4b.

$$C_{^{212}\mathrm{Pb}} = \frac{1}{1.42Q\eta_1\eta_2K_a}\left(0.1073N_2 - 0.105N_1\right), \tag{13}$$

$$C_{^{212}\mathrm{Bi}} = \frac{1}{1.42Q\eta_1\eta_2K_a}\left(0.1593N_1 - 0.0377N_2\right), \tag{14}$$

where η_1 is the counting efficiency (η_1=0.127), η_2 is the filtration efficiency (η_2=0.99), and K_a is the self-absorption factor of the filter membrane (K_a=0.97) [9, 10].

2.6 Evaluating indicator

2.6.1 Indicators for experimental- and simulation-error comparisons

The attached ^{212}Pb and ^{212}Bi abbreviations in the following text are written as ^{212}Pb and ^{212}Bi, respectively. Henceforth, progeny refers to the attached ^{212}Pb and ^{212}Bi. In this study, the alpha-spectrometer method mentioned in Sect. 2.5 was used to measure progeny concentrations with varying wind speeds and progeny-replenishment rates. The obtained experimental results (c_i^{e}) were then compared with the numerical simulation results (c_i^{s}) by calculating the relative deviation (RD). Verifying the uniformity of the progeny concentration through experimental research is difficult because it requires the simultaneous measurement of the progeny concentration at 27 spatial positions, as shown in Fig. 5. As a result, this study confirmed the consistency of progeny concentration between the simulation and experimentation at equilibrium. However, the uniformity of the progeny concentration between the simulation and experimentation at equilibrium has not yet been confirmed.

$$RD = \left|\frac{c_i^{\mathrm{e}} - c_i^{\mathrm{s}}}{c_i^{\mathrm{e}}}\right| \tag{15}$$

2.6.2 Performance-evaluation index of the ^{220}Rn chamber

The distribution of monitoring points in the ^{220}Rn chamber is illustrated in Fig. 5. Within the calibration chamber, the top, central, and bottom monitoring points were identified as T, C, and B, respectively. The coordinates of the central point are denoted as C22(0,0,0), which is the sampling area S_1. The distance between each site and the adjacent sites is 0.2 m. The sampling area S_2 is located at C12 in Fig. 5.

Two important indices, the progeny concentration level and uniformity of progeny concentrations, are crucial in determining the regulation ability. The mean progeny concentration ($\bar{C}$) at each monitoring point was calculated using Eq. (16). The uniformity of progeny concentrations within the ^{220}Rn

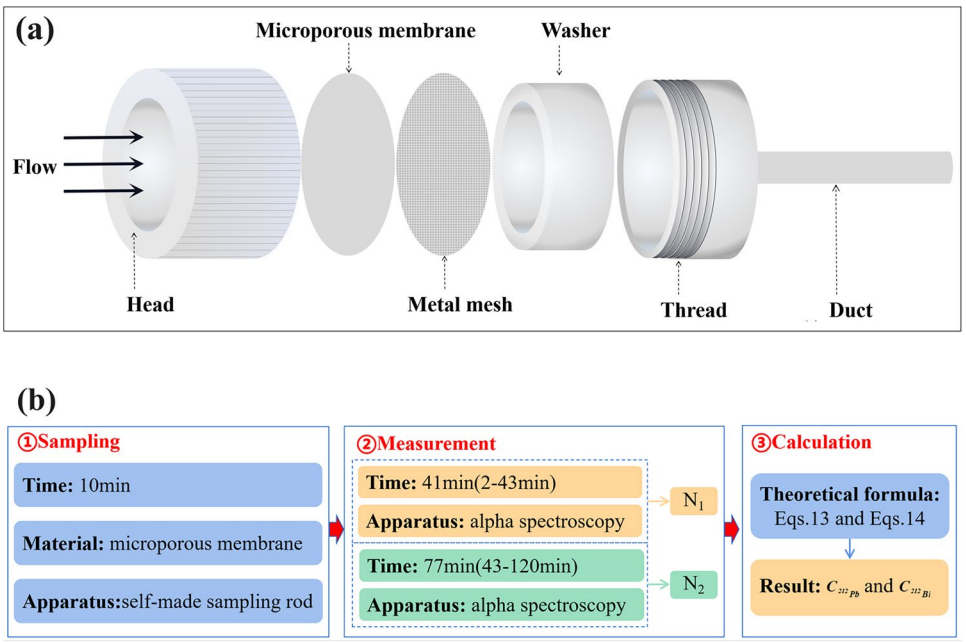

Fig. 4 **a** Structure of self-made sampling rod and **b** measurement procedure of progeny concentration

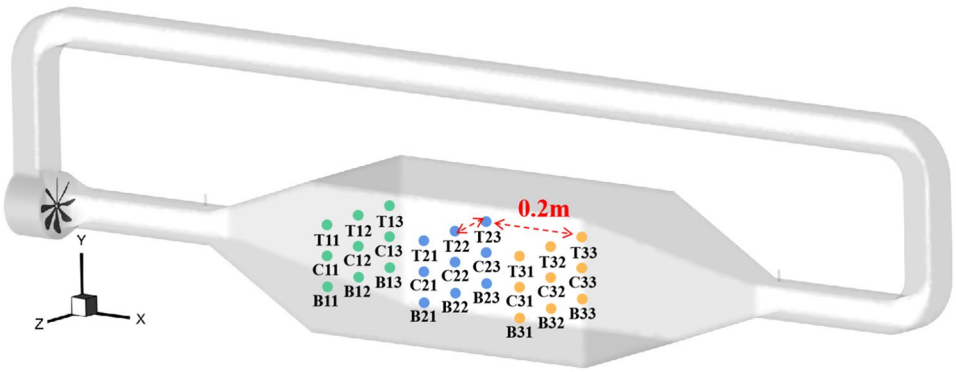

Fig. 5 (Color online) Distribution of monitoring sites in the ^{220}Rn chamber

chamber can be assessed using the relative standard deviation (*RSD*) at these monitoring points, as expressed in Eq. (17).

$$\bar{C} = \frac{1}{9}\sum_{1}^{9} c_i, \tag{16}$$

$$RSD = \frac{\sqrt{\frac{1}{9}\sum_{1}^{9}(c_i - \bar{c})^2}}{\bar{C}} \times 100\%, \tag{17}$$

where c_i denotes the concentration of ^{212}Pb or ^{212}Bi at the ith point.

3 Results and analysis

3.1 Comparison of the progeny concentration between experiment and simulation

To better illustrate the consistency of the simulation and experimental laws, validation experiments were conducted to ensure the reliability of the simulation data. The progeny concentration measured at sampling area S_1 in the experiment was compared with the progeny concentration at the same location in the CFD simulation. The simulation

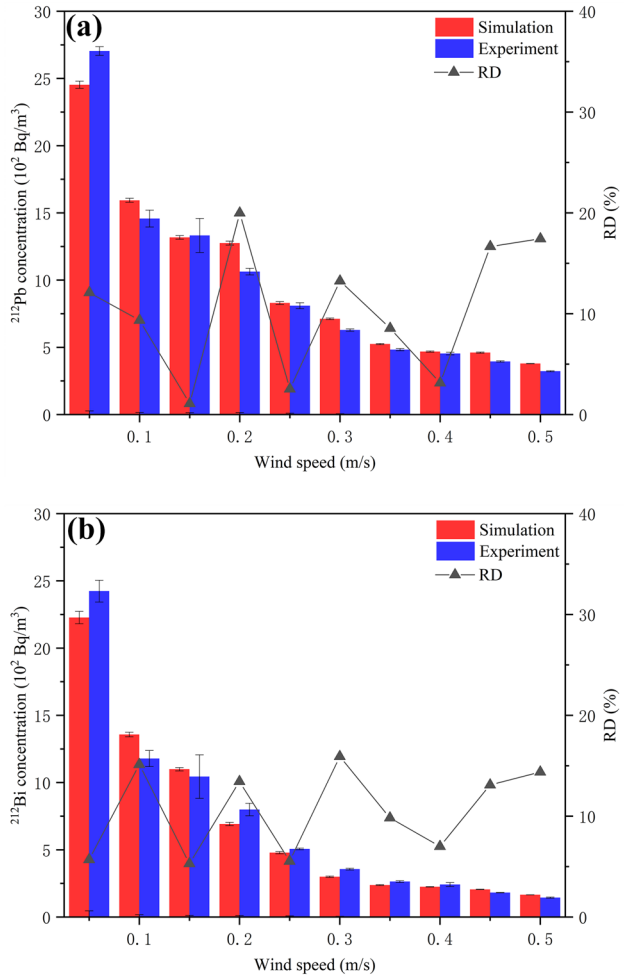

Fig. 6 The **a** ^{212}Pb concentration and **b** ^{212}Bi concentration obtained from measurements and simulation at the sampling area S_1

and experimental results were obtained by averaging the results of three experiments. Figure 6a and b shows the concentration values of the progeny obtained from the measurements and simulation. Figure 6a and b shows that as the wind speed gradually increased, the progeny concentration rapidly decreased, which is consistent with both the experimental and simulation results. Furthermore, the relative deviation (*RD*) between the simulated and experimental data for ^{212}Pb remained consistently below 20%, whereas that for ^{212}Bi remained below 15%. This unequivocally confirmed the reliability of the simulation.

3.2 Analysis of the impact of regulating parameters on the performance indicators of the ^{220}Rn chamber

This section analyzes the relationship between the performance indicators and wind speed, as well as the relationship between the performance indicators and complement rate of the progeny.

3.2.1 Effect of wind speed on the performance parameter of ^{220}Rn chamber

(1) Profile plots of the concentration of ^{212}Pb and ^{212}Bi.

Figure 7a illustrates the distribution of the progeny concentration at $x = -1$ m, −0.3 m, 0.3 m, and 1 m at different wind speeds, and Fig. 7b shows the progeny concentration profile at $z = 0$ m for various wind speeds. The progeny concentration profile at $x = 1$ m in Fig. 7a shows that the progeny concentration is significantly higher in the bottom section than in the middle and upper sections. Conversely, at $x = -1$ m in Fig. 7a, the progeny concentration in the middle was higher and indicated a more uniform distribution than that at $x = 1$ m. Furthermore, Fig. 7b demonstrates that the tail end of the progeny concentration distribution is more uniform than that at the front end. As the wind speed increases, the uniformity of the distribution improves.

Figure 8a displays the streamlines color-coded according to the velocity magnitude. Initially, progeny with a high concentration enters the calibration chamber from the inlet. Subsequently, the progeny circulate within the calibration chamber, particularly along the bottom wall, when the wind speed is low. Eventually, most of the progeny flow into the pipeline along the bottom wall of the calibration chamber, whereas a small fraction continues to circulate within the chamber.

Furthermore, the concentration profiles of ^{212}Pb and ^{212}Bi are higher below the inlet than at other places, particularly when the wind speed is relatively low. Figure 8b provides a detailed kinematic explanation of the motion characteristics of the progeny displayed in Fig. 8a, c. v_1 is the fluid velocity and v_2 represents the combined velocity between the initial velocity (v_G^*) and the velocity produced by gravity (v_G). Figure 8b shows that the progeny are initially injected (v_2^*) with a downward velocity (in the negative Y direction). When the injection velocity (v_2^*) is significantly higher than the fluid velocity (v_1), the progeny particles tend to accumulate in region B. This phenomenon is more likely to occur when the wind speed is low. This explains why the concentration of progeny at the bottom of the calibration chamber is higher than that in the other sections.

(2) Effect of wind speed on progeny concentration

The variation in the concentration of ^{212}Pb with wind speed at a fixed progeny-complement rate of 7 L/min is plotted in Fig. 9a. Figure 9a shows that the ^{212}Pb concentration decreases with wind speed from 0.05 to 0.5 m/s. When the wind speed is less than 0.25m/s, the progeny concentration is highly sensitive to changes in wind speed. When the wind speed exceeds 0.25 m/s, the sensitivity decreases. For a detailed analysis, at a wind speed of 0.05 m/s, the ^{212}Pb

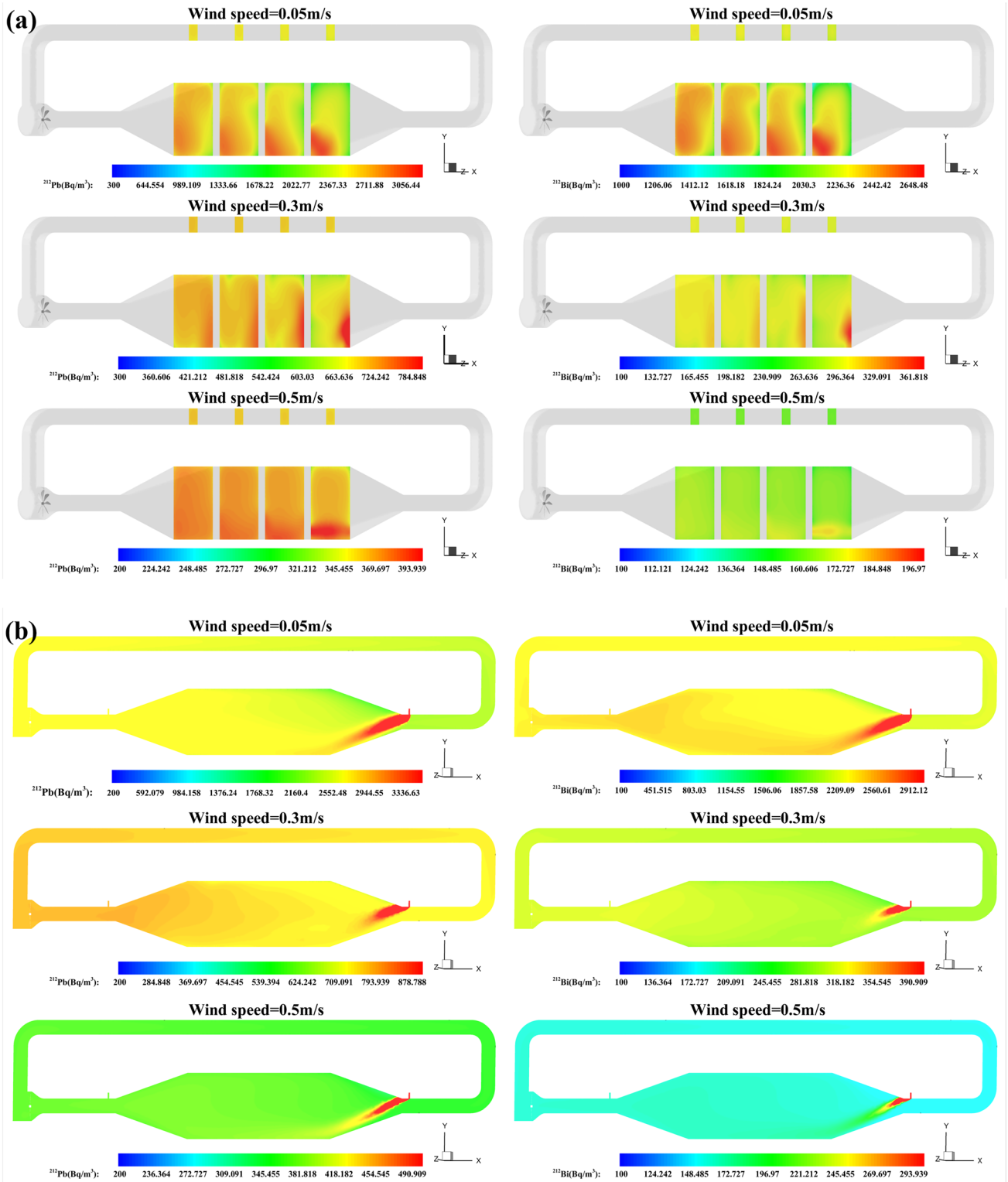

Fig. 7 (Color online) Simulated concentration profile of ^{212}Pb/^{212}Bi for different wind speeds for a fixed progeny-complement rate of 7 L/min at $x = -1$ m, −0.3 m, 0.3 m, 1 m, and $z = 0$ cm. The distribution of **a** ^{212}Pb concentration and **b** ^{212}Bi concentration in relation to wind speed, respectively

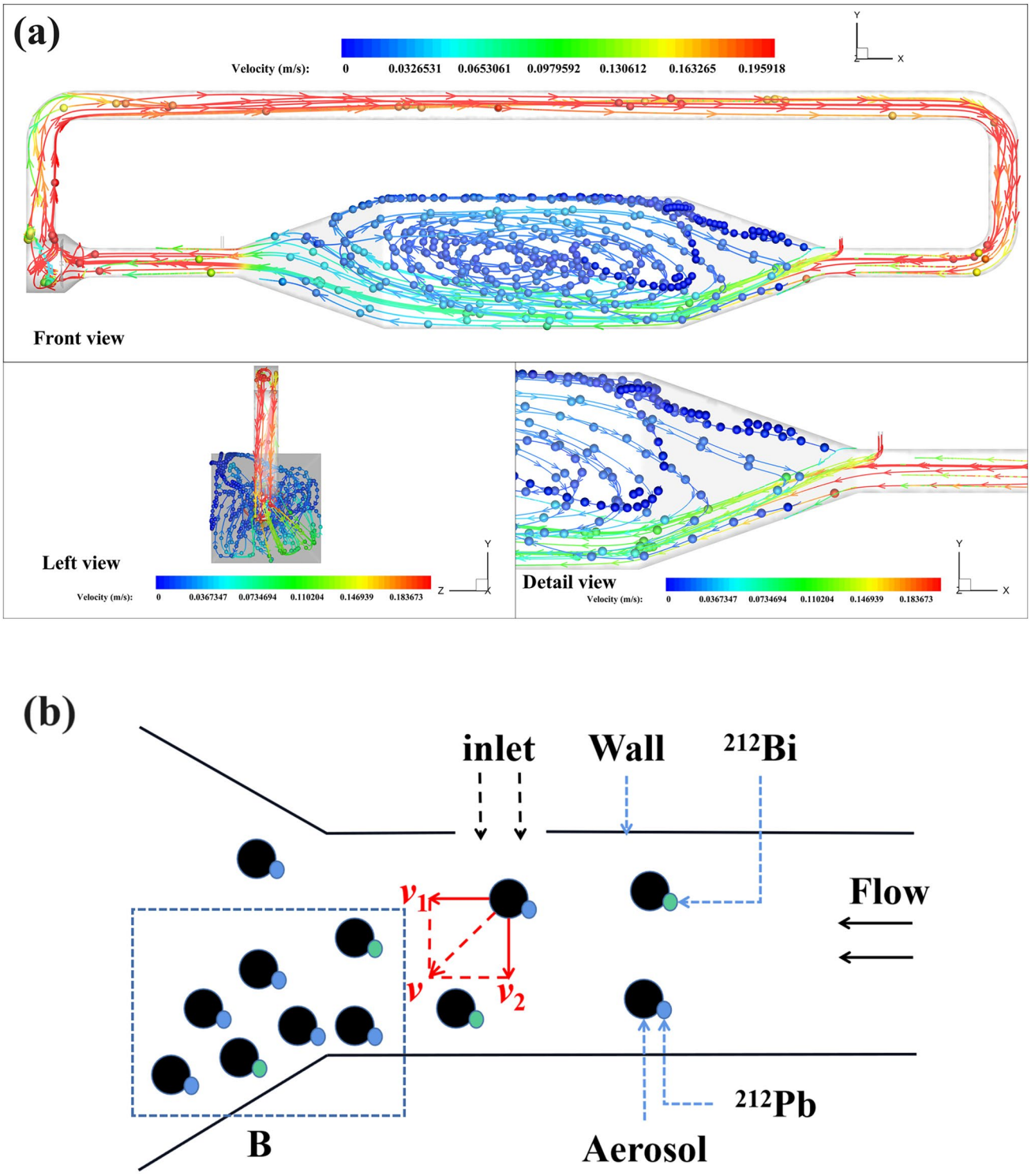

Fig. 8 (Color online) **a** Streamlines colored by the velocity magnitude (m/s) of flow for wind speed of 0.05 m/s. **b** Progeny velocity vector diagram around progeny-complement entrance area

concentration is 2513 Bq/m^3, and the ^{212}Pb concentration is 378 Bq/m^3 at a wind speed of 0.5 m/s. In comparison, the ^{212}Pb concentration in the latter is reduced to 15% of that in the former. In addition, at a wind speed of 0.05 m/s, the ^{212}Bi concentration is 2285 Bq/m^3, and the ^{212}Bi concentration is 165 Bq/m^3 at a wind speed of 0.5 m/s. In comparison, the

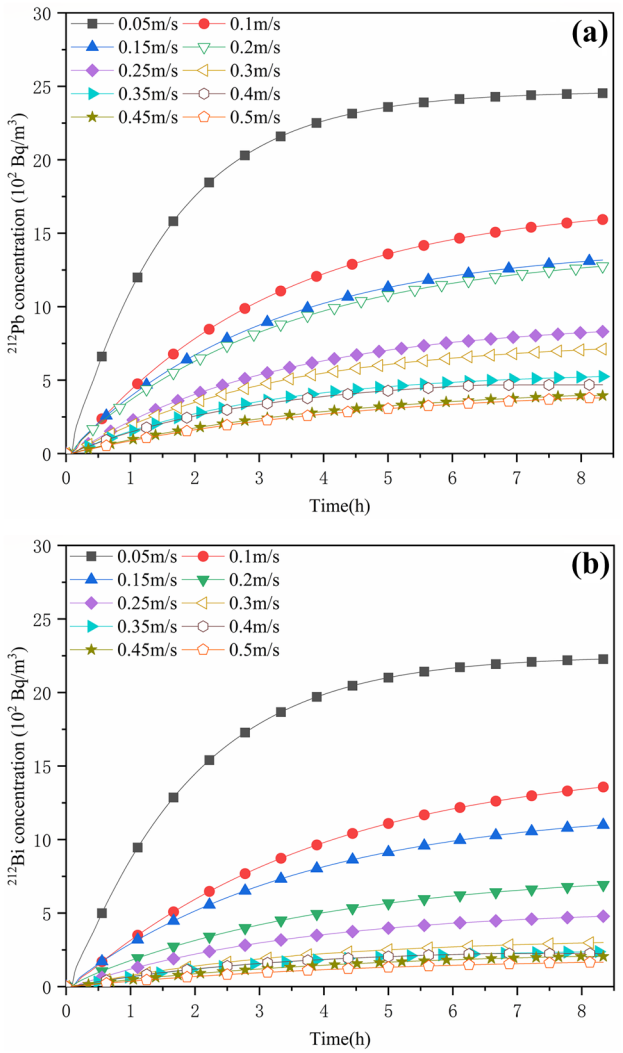

Fig. 9 (Color online) Variation of **a** ^{212}Pb concentration and **b** ^{212}Bi concentration with wind speed at a fixed progeny-complement rate of 7 L/min

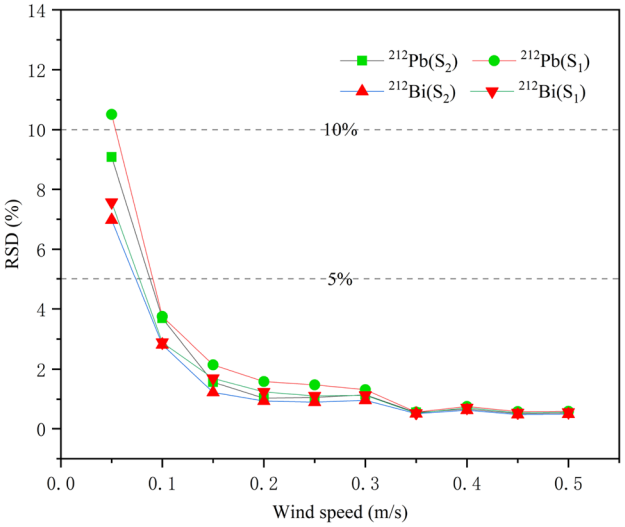

Fig. 10 (Color online) *RSD* of progeny with wind speed at a fixed progeny-complement rate of 7 L/min

^{212}Bi concentration of the latter is reduced to 7.2% of that of the former. Progeny concentration is greatly affected by wind speed. This is primarily because higher wind speeds result in a more pronounced deposition of progeny [9]. Therefore, wind speed significantly affects progeny concentration and is a key parameter in its regulation.

(3) Effect of wind speed on uniformity

Figure 7a and b in Sect. 3.2.1 qualitatively show that as the wind speed increases, the uniformity of the progeny concentration in the ^{220}Rn chamber gradually improves. In addition, Fig. 8 quantitatively shows the relationship between the uniformity of the progeny concentration and wind speed. Based on the results presented in Fig. 10, an increase in wind speed leads to a gradual decrease in the *RSD* of the progeny concentration. This decrease indicates an improvement in the uniformity of the progeny concentration within the ^{220}Rn chamber, which aligns with the conclusions presented in Sect. 3.2.1. Specifically, when the wind speed ranges from 0.05 to 0.50 m/s, the *RSD* of ^{212}Pb in sampling area S_1 decreases from 10.51 to 0.60%, whereas the *RSD* of ^{212}Bi decreases from 7.57 to 0.57%. Similarly, in sampling area S_2, the *RSD* of ^{212}Pb decreases from 9.08 to 0.54%, and the *RSD* of ^{212}Bi decreases from 7.97 to 0.51% within the same wind speed range. These significant changes in *RSD* indicate the strong influence of wind speed on the uniformity of progeny concentration. Notably, when the wind speed exceeds 0.2 m/s, it has little effect on the uniformity of the progeny concentration in the two sampled regions, with an *RSD* of 1.6%.

3.2.2 Effect of progeny-complement rate on performance parameter of ^{220}Rn chamber

(1) Profile plots of the concentration of ^{212}Pb and ^{212}Bi.

Section 3.2.1 shows that when the wind speed is 0.05 m/s, the progeny concentration gradient is the most obvious. Therefore, to clearly analyze the distribution of progeny concentration in Sect. 3.2.2, the wind speed in this section is set to 0.05 m/s. Figure 11a illustrates the distribution of progeny concentration at $x = -1$ m, -0.3 m, 0.3 m, and 1 m for different progeny-complement rates, and Fig. 11b shows the progeny concentration profile at $z = 0$ m for various progeny-complement rates. Compared with the middle and upper sections of the progeny concentration distribution at $x = 1$ m, the progeny concentration at the bottom is significantly higher, and at $x = -1$ m in Fig. 11a, the progeny concentration in the middle area is higher. Compared with

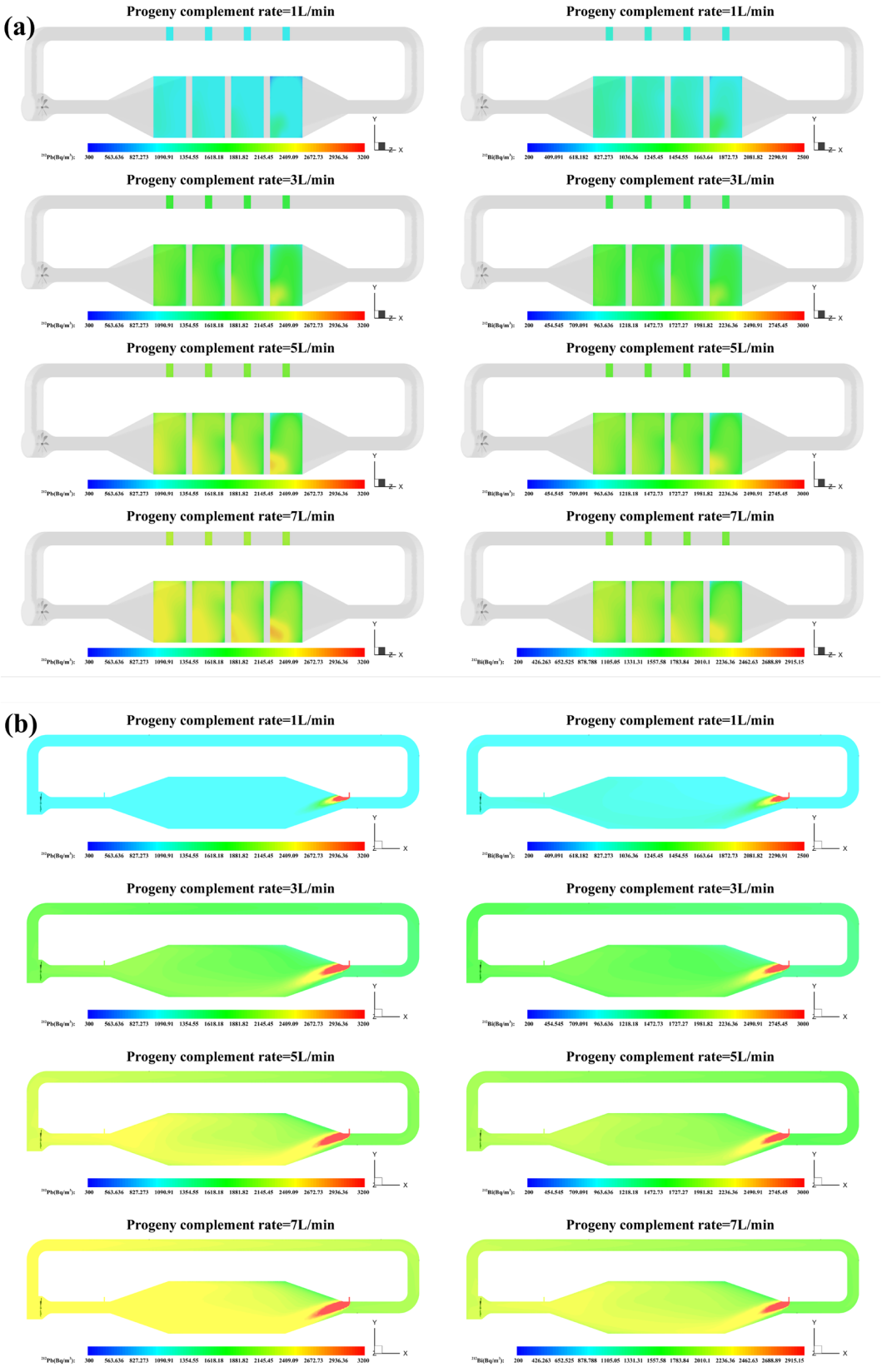

Fig. 11 (Color online) Simulated concentration profile of progeny for different progeny-complement rates for a fixed wind speed of 0.05 m/s at $x = -1$ m, -0.3 m, 0.3 m, 1 m, and $z = 0$ m. The distribution of **a** ^{212}Pb concentration and **b** ^{212}Bi concentration with progeny-complement rates respectively

the effect of wind speed on the progeny-complement rate mentioned in Sect. 3.2.1, the impact of wind speed on progeny concentration uniformity is significantly greater.

(2) Effect of progeny-complement rate on progeny concentration

The variation in ^{212}Pb concentration with the progeny-complement rate at a fixed wind speed of 0.05 m/s is plotted in Fig. 12a. Figure 12a and Figure 12b shows that the ^{212}Pb and ^{212}Bi concentrations gradually increase as the progeny-complement rate increases from 1 to 7 L/min. The concentration of ^{212}Pb increased from 1132 Bq/m^3 to 2513 Bq/m^3, an increase of 122%, while the concentration of ^{212}Bi increased from 981 Bq/m^3 to 2285 Bq/m^3, an increase of 133%. Notably, Eqs. (9) and (10) show that when the progeny-complement rate increases, the progeny concentration in the air charged into the ^{220}Rn chamber from the inlet decreases. However, the progeny-complement amount per unit time increases; thus, the progeny concentration level can be effectively improved. Therefore, in addition to wind speed, the progeny-complement rate is a key parameter for regulating progeny concentration.

(3) Effect of progeny-complement rate on uniformity

Figure 11a in Sect. 3.2.2 qualitatively show that as the progeny complement increases, the uniformity of the progeny concentration change in the ^{220}Rn chamber is not obvious. In addition, Fig. 13 quantitatively shows the relationship between the uniformity of the progeny concentration and progeny-complement rate. Based on the data presented in Fig. 13, the *RSD* of the ^{212}Pb concentration ranges from 8.90 to 10.51% in sampling area S1, whereas the *RSD* of the ^{212}Bi concentration ranges from 7.55 to 7.87% in the same area. In sampling area S2, the *RSD* of the ^{212}Pb concentration varies between 8.40% and 8.92%, whereas the *RSD* of ^{212}Bi concentration ranges from 6.97 to 7.45%. The *RSD* value of the progeny concentration exhibits little change and was relatively stable. Thus, we can conclude that the impact of the progeny-complement rate on progeny concentration uniformity is negligible compared with the influence of wind speed.

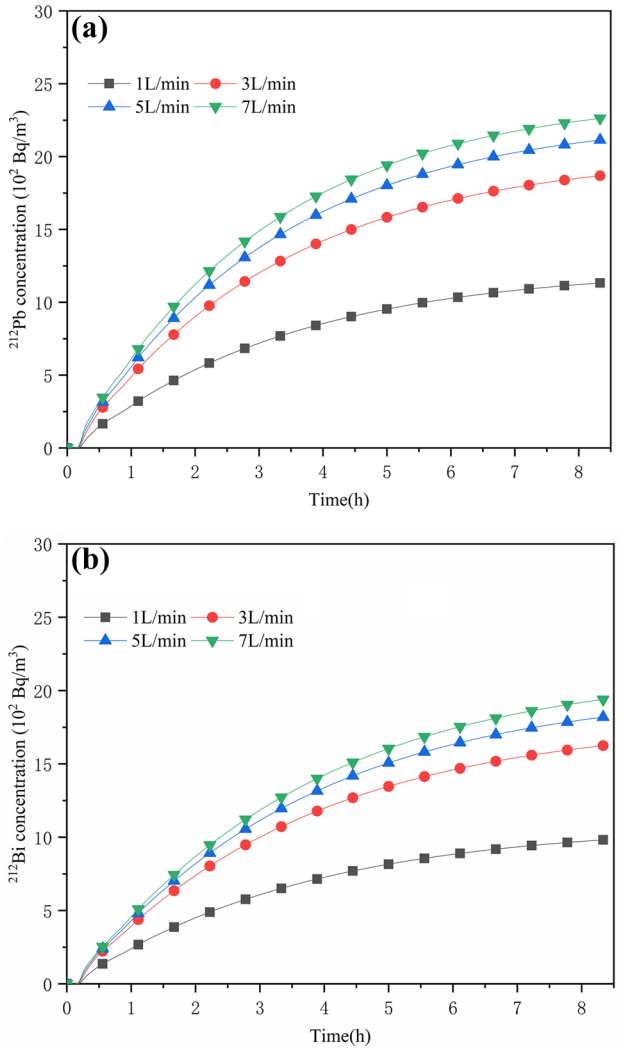

Fig. 12 (Color online) Variation of **a** ^{212}Pb concentration and **b** ^{212}Bi concentration with progeny-complement rate at a fixed wind speed of 0.05 m/s

4 Comprehensive analysis on optimization of performance parameters of ^{220}Rn chamber

In Sect. 3, the influence of two adjustment parameters, wind speed and progeny-complement rate, on two performance indexes of the ^{220}Rn chamber, uniformity and concentration

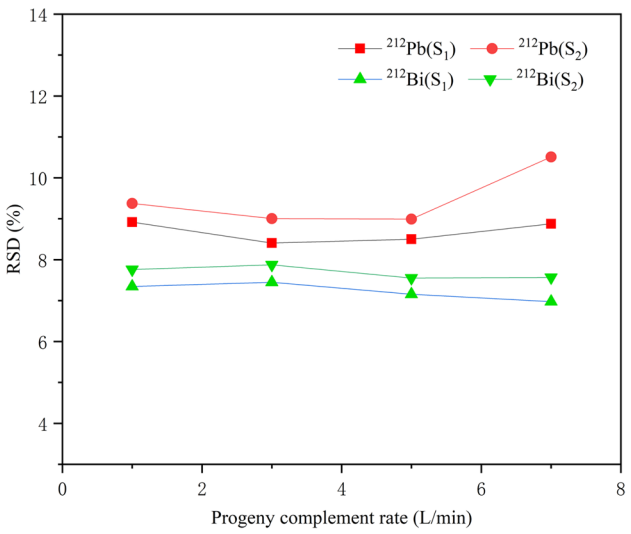

Fig. 13 *RSD* of progeny with progeny-complement rate at a fixed wind speed of 0.05 m/s

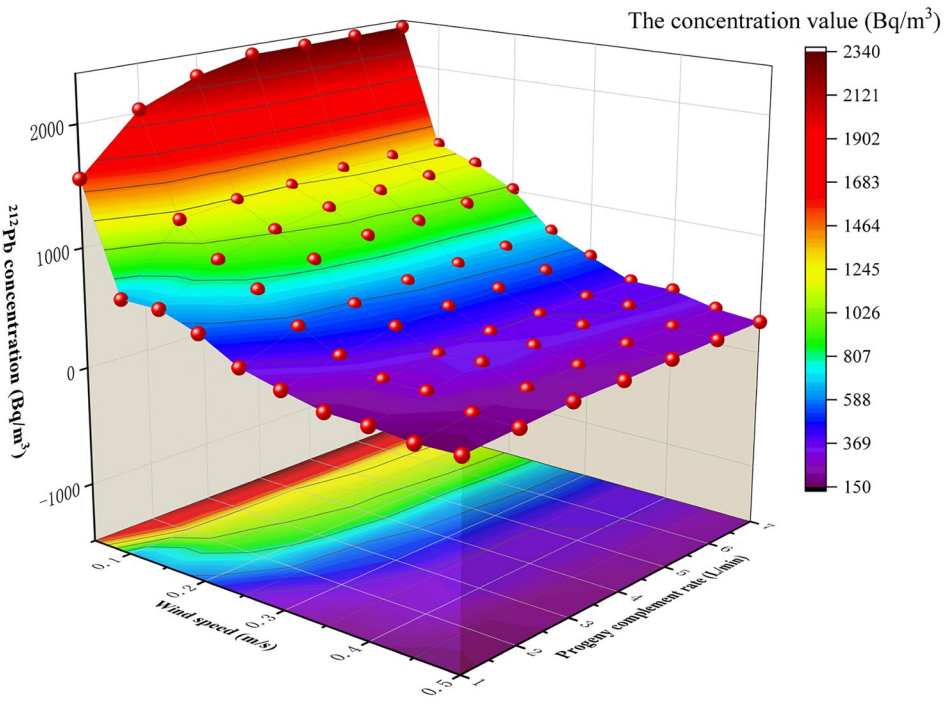

(a)

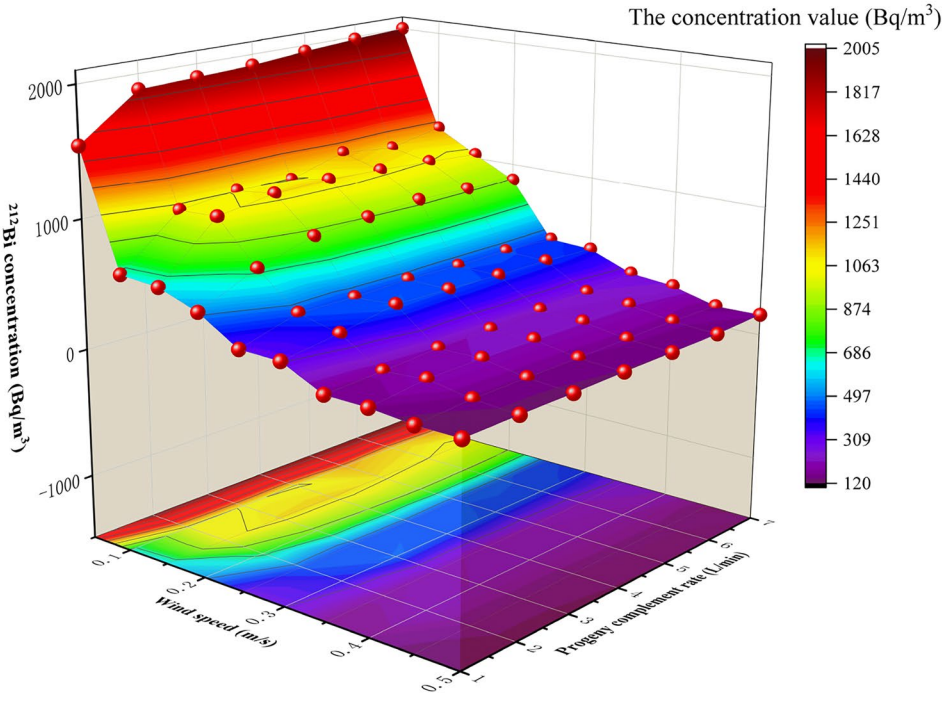

(b)

Fig. 14 (Color online) **a** ^{212}Pb concentration and **b** ^{212}Bi concentration under different wind speed and progeny-complement rate

level of the progeny concentration, are analyzed. However, this analysis needs to be considered comprehensively to achieve good uniformity of progeny concentration and the specified concentration level. This section presents a comprehensive analysis of the adjustment of progeny concentration levels using wind speed and the progeny-complement rate.

In the progeny-sampling experiment, the ideal progeny concentration uniformity in the sampling area is within 5%. If this is not achievable, it should be less than 10%. Figure 14a and b shows the concentration values of ^{212}Pb and ^{212}Bi, respectively, under different wind speeds and progeny-complement rates. When the wind speed exceeds 0.1m/s and the progeny-complement rate ranges from 1 to 7 L/min, the ^{212}Pb concentration ranges from 163 to 1305 Bq/m^3, whereas the concentration of ^{212}Bi ranges from 123 to 1203 Bq/m^3. As indicated in Sect. 3.2.1, the progeny concentration uniformity in both sampling areas is less than 5%. Thus, sampling could proceed. However, when the wind speed is below 0.1m/s and the progeny-complement rate ranges from 1 to 7 L/min, the concentration of ^{212}Pb varies from 1305 Bq/m^3 to 2338 Bq/m^3, and the concentration of ^{212}Bi varies from 1203 Bq/m^3 to 2001 Bq/m^3. Section 3.2.1 reveals that the progeny concentration uniformity in the sampling area S_1 exceeds 5%, particularly at a wind speed of 0.05m/s, where it surpasses 10%. Conversely, the progeny concentration uniformity in sampling area S_2 was less than 10%, and the flow field remains stable, making it more suitable for sampling.

5 Conclusion

In this study, we utilized CFD to conduct a numerical simulation and analyze the correlation between progeny concentration level, progeny concentration uniformity, wind speed, and progeny-complement rate. To enhance the accuracy of the model, physical laws such as progeny-deposition and decay laws were incorporated. Additionally, the model was validated through experiments, establishing a solid groundwork for simulating and analyzing the spatial distribution of progeny concentration. The findings of this study offer reliable theoretical guidance for regulating progeny concentration and ensuring the accurate sampling of progeny concentration.

The next step in our research will be to conduct-related studies on the simultaneous regulation of ^{220}Rn and its progeny, based on the results of this study. The simultaneous regulation of ^{220}Rn and its progeny is the key technology to realizing the measurement of ^{220}Rn and its progeny. Compared with the use of only the concentration regulation for the ^{220}Rn progeny, the key regulation parameters in the simultaneous regulation of ^{220}Rn and its progeny are more numerous, and their workload is greatly increased. The numerical calculation method, which relies on CFD, has a limited ability to provide rapid predictions owing to its reliance on iterative algorithms. Therefore, the subsequent step will involve conducting related research on the concurrent regulation of ^{220}Rn and its progeny using artificial intelligence, with the aim of establishing a rapid prediction method for their concurrent regulation. In particular, the focus should be on devising a method that allows for the reverse prediction of regulatory parameters when the target state is known. These studies are significant for further improving the control level of ^{220}Rn chambers and the measurement level of ^{220}Rn and its progeny.

Author contributions All authors contributed to the study conception and design. Material preparation, data collection, and analysis were performed by Shao-Hua Hu, Xiang-Yu Xu, and Jian-Kai Wang. The first draft of the manuscript was written by Shao-Hua Hu, and all authors commented on previous versions of the manuscript. All authors read and approved the final manuscript.

Data availibility statement The data that support the findings of this study are openly available in Science Data Bank at https://cstr.cn/31253.11.sciencedb.j00186.00107 and https://doi.org/10.57760/sciencedb.j00186.00107.

Declarations

Conflict of interest The authors declare that they have no conflict of interest.

References

1. X. Deng, B. Yu, H. Wu et al., High-efficiency radon adsorption by nickel nanoparticles supported on activated carbon. New J. Chem. **46**, 9222–9228 (2022). https://doi.org/10.1039/d2nj00862a
2. X. Deng, Y. Liao, M. Wang et al., Investigation of the effect of the key pore size on the radon adsorption performance by combining grand canonical Monte Carlo and activated carbon modification experiments. Appl. Surf. Sci. **643**, 158730 (2024). https://doi.org/10.1016/j.apsusc.2023.158730
3. T.K. Agarwal, B.K. Sahoo, M. Kumar et al., A computational fluid dynamics code for aerosol and decay-product studies in indoor environments. J. Radioanal. Nucl. Ch. **330**, 1347–1355 (2021). https://doi.org/10.1007/s10967-021-07877-8
4. L. Zhang, W. Zhuo, Q. Guo et al., An instrument for measuring the unattached fraction of radon progeny with etched track detectors. J. Radiol. Prot. **30**, 607 (2010). https://doi.org/10.1088/0952-4746/30/3/014
5. T. Asano, K. Sato, J.I. Onodera, United Nations scientific committee on the Effects of Atomic Radiation 2000 report. Jpn. J. Health. Phys. **36**, 149–158 (2001). https://doi.org/10.5453/jhps.36.149
6. Q. Guo, J. Cheng, Indoor thoron and radon concentrations in Zhuhai. China. J. Nucl. Sci. Technol. **42**, 588–591 (2005). https://doi.org/10.1080/18811248.2004.9726425
7. J. Hu, Y. Wu, M.A. Saputra et al., Radiation exposure due to ^{222}Rn, ^{220}Rn and their progenies in three metropolises in China and Japan with different air quality levels. J. Environ. Radioactiv. **244**, 106830 (2022). https://doi.org/10.1016/j.jenvrad.2022.106830
8. S.D. Kanse, B.K. Sahoo, J.J. Gaware et al., A study of thoron exhalation from monazite-rich beach sands of High Background

Radiation Areas of Kerala and Odisha. India. Environ. Earth. Sc. **75**, 1–10 (2016). https://doi.org/10.1007/s12665-016-6279-9
9. Z.Z. He, D.T. Xiao, L.D. Lv et al., Controlling ^{212}Bi to ^{212}Pb activity concentration ratio in thoron chambers. J. Environ. Radioactiv. **178**, 77–83 (2017). https://doi.org/10.1016/j.jenvrad.2017.07.011
10. J. Lin, D. Xiao, Z. He et al., Regulation and control methods for the unattached fraction of ^{220}Rn progeny in a ^{220}Rn progeny chamber. J. Environ. Radioactiv. **235**, 106653 (2021). https://doi.org/10.1016/j.jenvrad.2021.106653
11. Z. He, D. Xiao, L. Lv et al., Stable control of thoron progeny concentration in a thoron chamber for calibration of active sampling monitors. Radiat. Meas. **102**, 27–33 (2017). https://doi.org/10.1016/j.radmeas.2017.02.013
12. H. Huang, G. Li, Q. Zhou et al., Study of the cyclic loss rate of ^{220}Rn progeny in a ^{220}Rn chamber by an airflow model. J. Radioanal. Nucl. Ch. **332**, 2633–2641 (2023). https://doi.org/10.1007/s10967-023-08930-4
13. Y. Ye, W. Liu, S. Li et al., A laboratory method for concurrently determining diffusion migration parameters and water saturation effects of thoron in uranium tailings. Chemosphere **249**, 126520 (2020). https://doi.org/10.1016/j.chemosphere.2020.126520
14. D. Tisha, G. Indranil, Prospective of employing high porosity open-cell metal foams in passive cryogenic radiators for space applications. In IOP Conference Series: Mater. Sci. Eng. **171**, 012048 (2017). https://doi.org/10.1088/1757-899X/171/1/012048
15. W. Choi, S. Hu, M. He et al., studied the Neighborhood-scale air quality impacts of emissions from motor vehicles and aircrafts. Atmos. Environ. **80**, 310–321 (2013). https://doi.org/10.1016/j.atmosenv.2013.07.043
16. C. Kim, K. Zhou, Analysis of automotive disc brake squeal considering damping and design modifications for pads and a disc. Int. J. Auto. Tech-kor. **17**, 213–223 (2016). https://doi.org/10.1007/s12239-016-0021-1
17. K. Tsutsumi, S. Watanabe, S.I. Tsuda et al., Cavitation simulation of automotive torque converter using a homogeneous cavitation model. Eur. J. Mech. B-Fluids **61**, 263–270 (2017). https://doi.org/10.1016/j.euromechflu.2016.09.001
18. Z.R. Zhang, L. Hui, S.P. Zhu et al., Application of CFD in ship engineering design practice and ship hydrodynamics. J. Hydrodyn. Ser. B **18**, 315–322 (2006). https://doi.org/10.1016/S1001-6058(06)60072-3
19. S. Song, Y.K. Demirel, M. Atlar et al., Validation of the CFD approach for modelling roughness effect on ship resistance. Ocean Eng. **200**, 107029 (2020). https://doi.org/10.1016/j.oceaneng.2020.107029
20. D. Kim, S. Song, T. Tezdogan, Free running CFD simulations to investigate ship manoeuvrability in waves. Ocean Eng. **236**, 109567 (2021). https://doi.org/10.1016/j.oceaneng.2021.109567
21. B. Amblard, R. Singh, E. Gbordzoe et al., CFD modeling of the coke combustion in an industrial FCC regenerator. Chem. Eng. Sci. **170**, 731–742 (2017). https://doi.org/10.1016/j.ces.2016.12.055
22. N. Anna, D.W. Park, T. Charinpanitkul et al., Numerical analysis on premixed combustion of H_2-$SiCl_4$-Air system to prepare SiO_2 Particles. J. Ind. Eng. Chem. **18**, 509–512 (2012). https://doi.org/10.1016/j.jiec.2011.11.071
23. K. Ahookhosh, M. Saidi, H. Aminfar et al., Dry powder inhaler aerosol deposition in a model of tracheobronchial airways: validating CFD predictions with in vitro data. Int. J. Pharm. **587**, 119599 (2020). https://doi.org/10.1016/j.ijpharm.2020.119599
24. L.L.X. Augusto, G.C. Lopes, J.A.S. Gonçalves, A CFD study of deposition of pharmaceutical aerosols under different respiratory conditions. Braz. J. Chem. Eng. **33**, 549–558 (2016). https://doi.org/10.1590/0104-6632.20160333s20150100
25. Y. Shi, J. Wei, J. Qiu et al., Numerical study of acoustic agglomeration process of droplet aerosol using a three-dimensional CFD-DEM coupled model. Powder Technol. **362**, 37–53 (2020). https://doi.org/10.1016/j.powtec.2019.12.017
26. T. Zhenbo, Z. Wenqi, Y. Aibing et al., CFD-DEM investigation of the effect of agglomerate-agglomerate collision on dry powder aerosolisation. J. Aerosol Sci. **92**, 109–121 (2016). https://doi.org/10.1016/j.jaerosci.2015.11.005
27. T.K. Agarwal, B.K. Sahoo, M. Joshi et al., CFD simulations to study the effect of ventilation rate on ^{220}Rn concentration distribution in a test house. Radiat. Phys. Chem. **162**, 82–89 (2019). https://doi.org/10.1016/j.radphyschem.2019.04.018
28. T.K. Agarwal, J.J. Gaware, B.K. Sapra, A CFD-based approach to optimize operating parameters of a flow-through scintillation cell for measurement of ^{220}Rn in indoor environments. Environ. Sci. Pollut. R. **29**, 16404–16417 (2022). https://doi.org/10.1007/s11356-021-16780-4
29. Y. Ye, L.K. Chung, Q. Zhou et al., Evaluation of ^{222}Rn and ^{220}Rn discriminating concentration measurements with pinhole-based twin cup dosimeters using computational fluid dynamics simulations. Radiat. Meas. **134**, 106369 (2020). https://doi.org/10.1016/j.radmeas.2020.106369
30. T.K. Agarwal, S.D. Kanse, R. Mishra et al., A CFD based approach to assess the effect of environmental parameters on decay product-aerosol attachment coefficient. J. Radioanal. Nucl. Ch. **331**, 3563–3570 (2022). https://doi.org/10.1007/s10967-022-08402-1
31. K. Akbari, J. Mahmoudi, M. Ghanbari, Influence of indoor air conditions on radon concentration in a detached house. J. Environ. Radioactiv. **116**, 166–173 (2013). https://doi.org/10.1016/j.jenvrad.2012.08.013
32. W. Zhou, T. Iida, J. Moriizumi et al., Simulation of the concentrations and distributions of indoor radon and thoron. Radiat. Prot. Dosim. **93**, 357–367 (2001). https://doi.org/10.1093/oxfordjournals.rpd.a006448
33. T.K. Agarwal, B.K. Sahoo, J.J. Gaware et al., CFD based simulation of thoron (^{220}Rn) concentration in a delay chamber for mitigation application. J. Environ. Radioactiv. **136**, 16–21 (2014). https://doi.org/10.1016/j.jenvrad.2014.05.003
34. P.M. Dieguez-Elizondo, T. Gil-Lopez, P.G. O'Donohoe et al., An analysis of the radioactive contamination due to radon in a granite processing plant and its decontamination by ventilation. J. Environ. Radioactiv. **167**, 26–35 (2017). https://doi.org/10.1016/j.jenvrad.2016.11.016
35. H. Jun, Y. Guosheng, H. Miklós et al., Numerical modeling of the sources and behaviors of ^{222}Rn, ^{220}Rn and their progenies in the indoor environment-A review. J. Environ. Radioactiv. **123**, 114–126 (2018). https://doi.org/10.1016/j.jenvrad.2018.03.006
36. W. Li, Q. Zhou, Z. He et al., optimized a thoron progeny compensation system in a thoron calibration chamber. J. Radioanal. Nucl. Ch. **324**, 1255–1263 (2020). https://doi.org/10.1007/s10967-020-07180-y
37. A.C. Lai, W.W. Nazaroff, Modeling indoor particle deposition from turbulent flow onto smooth surfaces. J. Aerosol Sci. **31**, 463–476 (2000). https://doi.org/10.1016/S0021-8502(99)00536-4
38. Y. Ye, L.K. Chung, Q. Zhou et al., Evaluation of ^{222}Rn and ^{220}Rn discriminating concentration measurements with pinhole-based twin cup dosimeters using computational fluid dynamics simulations. Radiat. Meas. **134**, 106369 (2020). https://doi.org/10.1016/j.radmeas.2020.106369